

QR-RECURSIVE COMPRESSION OF VOLUME INTEGRAL EQUATIONS FOR ELECTROMAGNETIC SCATTERING BY LARGE METASURFACES

VINCENZO MOTTOLA¹, ANTONELLO TAMBURRINO¹, LUCA BERGAMASCHI²,
ANDREA G. CHIARIELLO³, EMANUELE CORSARO⁴, CARLO FORESTIERE⁴,
GUGLIELMO RUBINACCI^{4,5} AND SALVATORE VENTRE¹

Abstract. In this paper, a novel QR decomposition-based compression scheme is combined with a volume integral equations method for the fast and efficient numerical computation of the scattering of electromagnetic fields from large scale metasurfaces, via an iterative approach.

The underlying problem is of a multiscale nature. Indeed, these metasurfaces are made of a large collection of interacting sub-wavelength scatterers, thus making the numerical computation of the solution very challenging.

More specifically, the paper proposes a tailored version of a QR decomposition-based compression for a volume integral equation, together with a proper preconditioner that exploits the geometrical structure of the array, in order to achieve a fast and accurate iterative solver, in view of realistic applications. Numerical examples prove the effectiveness of the method in efficiently modeling metasurfaces made by thousands of particles.

Keywords: Metasurfaces, Electromagnetic Scattering, Volume Integral Equations, Fast Numerical Methods, Iterative Methods.

1. INTRODUCTION

Metasurfaces, composed of interacting subwavelength scatterers operating near resonance [1], offer a powerful platform for controlling electromagnetic waves. By carefully designing the geometry and arrangement of these scatterers, metasurfaces enable the engineering of a wide range of effective constitutive relations [2]. Their versatility has driven advances in applications such as analog computing [3], biosensing [4], and imaging [5]. Efficient and accurate simulation of metasurfaces

¹Department of Electrical and Information Engineering, University of Cassino and Southern Lazio, Via Gaetano di Biasio 43, 03043 Cassino, Italy.

² Department of Civil Environmental and Architectural Engineering University of Padova, via Marzolo 9, 35131 Padova

³ Department of Engineering, Università degli Studi della Campania “Luigi Vanvitelli”, via Roma 29, 81031 Aversa, Italy

⁴ Department of Electrical Engineering and Information Technology, Università degli Studi di Napoli Federico II, 80138 Napoli, Italy

⁵ Consorzio CREATE, 80125 Napoli, Italy

Email: antonello.tamburrino@unicas.it

is essential for understanding their fundamental properties [6] and for optimizing their performance in practical implementations [7].

Metasurfaces design often relies on the “unit cell” approximation [8, 9, 10]. This approach constructs a library of the electromagnetic response of meta-atoms, such as disks, pillars, or nanofins, as a function of a design parameter, like the disk radius, pillar height, or the nanofin orientation, assuming the structure to be locally periodic. Then, the contributions of the different “unit cell” are combined by linear superposition. Unfortunately, the “unit cell” approach has several limitations: the most critical limitation is the assumption that the interaction between adjacent meta-atoms is assumed equal to that in periodic arrays, which necessitates a slowly changing structure. This constraint limits the design space, resulting in narrow-bandwidth operation, low efficiencies, and many types of non-ideality.

General-purpose electromagnetic simulation tools, based on either *integral* or *differential* formulations, face significant challenges in the simulation of metasurfaces [6]. Differential formulations, including finite-element methods and finite-difference methods, are easy to implement and result in sparse matrices but require truncation of the computational domain through the introduction of convenient boundary conditions [11]. Among them, the finite-difference time-domain (FDTD) method [12, 13, 14] is widely used to model metasurfaces. However, the finite resolution leads to inaccuracies in wave speed, resulting in phase accumulation errors as the size of the scattering region increases. Hence, even though the complexity of FDTD simulations nominally increases linearly with the size of the array, maintaining a fixed error requires increasing the resolution [15, 13]. This makes the approach prohibitive when applied using traditional computing platforms, requiring massive GPU parallelization to be viable [16].

Volume Integral formulations (e.g. [17, 18]) are appealing because they define the unknowns only within the objects’ volumes, and naturally satisfy radiation conditions at infinity. In addition, contrarily to *surface* formulations [19, 20] they also allow to treat inhomogeneous meta-atoms. However, they usually involve large dense matrices, which are computationally demanding to store and invert. Moreover, these matrices are often ill-conditioned, which can hinder the efficiency of iterative solvers such as GMRES.

To address these limitations, in this work we combine the volume integral formulation presented in [17, 18] with a QR compression scheme and a dedicated preconditioner. QR factorization methods are not new in computational electromagnetics, having been successfully applied to surface integral equation methods [21] and volume integral magnetoquasistatic formulations [22, 23]. In this case, both the compression scheme and the preconditioner are specifically designed for multi-scale collections of interacting meta-atoms, grouping basis functions by meta-atom at the finest-level group. The proposed method represents a first and key contribution in view of the simulation of suitable large-scale electromagnetic problems where the scatterer extends for thousands of wavelengths. Indeed, this method

can be easily coupled with Butterfly-Acceleration methods to tackle large-scale electromagnetic problems [24, 25].

The paper is organized as follows: in Section 2 the mathematical formulation of VIE for the problem of interest is presented; in Section 3 the numerical counterpart of the continuous model is detailed; in Section 4 the iterative method and the preconditioner employed in the computations are presented, while in Section 5 the compression method is detailed. Finally, in Section 6 some numerical examples on realistic configurations are reported and in Section 7 the conclusions are drawn.

2. MATHEMATICAL MODEL

In this Section the mathematical model represented by the source integral volume formulation is briefly summarized (see [17, 18, 26] for further details).

The underlying integral formulation is expressed in terms of equivalent sources. Specifically, the unknown is the polarization current density \mathbf{J} induced in the dielectrics. It is assumed that: (i) the region Ω occupied by the dielectrics consists of one or more bounded Lipschitz domains of \mathbb{R}^3 , (ii) dielectric materials are linear and non-spatially dispersive, (iii) the dielectric materials are homogeneous in each connected component of Ω , (iv) magnetic materials are not present, (v) the fields are computed in time-harmonic operations at the angular frequency ω (the $e^{j\omega t}$ time behavior is assumed) and (vi) no source charges are present in any possible cavity of Ω .

In addition, for the sake of generality, conductive materials may be present. In this latter case, Ω is the region occupied by the conducting materials, too, the conducting materials are linear, non-spatially dispersive, and homogeneous in each connected component of Ω . In typical dielectric materials the electrical conductivity is vanishing, while the dielectric permittivity may have a non-vanishing imaginary part, in case of dielectric losses.

Hereafter, Σ_i represents the i -th connected component of $\partial\Omega$.

The unknown of the integral formulation is, therefore, the sum of the polarization current density and of the (electrical) conduction current density, i.e.

$$\mathbf{J}(\mathbf{r}) = [\sigma(\mathbf{r}) + j\omega\varepsilon_0\chi(\mathbf{r})] \mathbf{E}(\mathbf{r}), \text{ in } \Omega, \quad (2.1)$$

where σ is the electrical conductivity, χ is the dielectric susceptibility, ε_0 is the dielectric permittivity of the free-space

In general, \mathbf{J} is an element of $H(\text{div}; \Omega)$, the functional space of div-conforming vector fields:

$$H(\text{div}; \Omega) = \{\mathbf{v} \in \mathbb{L}^2(\Omega) : \nabla \cdot \mathbf{v} \in L^2(\Omega)\}. \quad (2.2)$$

In the specific case, \mathbf{J} is also a divergence free vector and its net flux on each connected component Σ_i of the boundary is vanishing, because materials are homogeneous in each connected component of Ω and the cavities of Ω are free from

source charges (see assumptions (iii) and (vi)). Thus, \mathbf{J} is an element of the following solution space:

$$H = \{\mathbf{v} \in H(\text{div}; \Omega) : \nabla \cdot \mathbf{v} = 0 \text{ in } \Omega, \int_{\Sigma_i} \mathbf{v} \cdot \hat{\mathbf{n}} dS = 0, \forall i\}. \quad (2.3)$$

The unknown \mathbf{J} satisfies the following integral equation:

$$\begin{aligned} & [\sigma(\mathbf{r}) + j\omega\chi(\mathbf{r})\varepsilon_0]^{-1} \mathbf{J}(\mathbf{r}) + j\omega\mu_0 \int_{\Omega} \mathbf{J}(\mathbf{r}') g(\mathbf{r} - \mathbf{r}') d\tau' \\ & + \frac{1}{j\omega\varepsilon_0} \nabla \int_{\partial\Omega} (\mathbf{J} \cdot \hat{\mathbf{n}})(\mathbf{r}') g(\mathbf{r} - \mathbf{r}') dS' = \mathbf{E}_0(\mathbf{r}), \text{ in } \Omega \end{aligned} \quad (2.4)$$

In equation (2.4) μ_0 is the magnetic permeability of the free-space, $g(\mathbf{r}) \triangleq e^{-jkr} / (4\pi r)$ is the scalar free space Green's function, $k = \omega\sqrt{\varepsilon_0\mu_0}$ is the free-space wavenumber, and \mathbf{E}_0 is the applied electric field.

Equation (2.4) in the weak form is:

$$\begin{aligned} & \int_{\Omega} \mathbf{J}'(\mathbf{r}) \cdot [\sigma(\mathbf{r}) + j\omega\chi(\mathbf{r})\varepsilon_0]^{-1} \mathbf{J}(\mathbf{r}) d\tau \\ & + j\omega\mu_0 \int_{\Omega} \int_{\Omega} \mathbf{J}'(\mathbf{r}) \cdot \mathbf{J}(\mathbf{r}') g(\mathbf{r} - \mathbf{r}') d\tau' d\tau \\ & + \frac{1}{j\omega\varepsilon_0} \int_{\partial\Omega} \int_{\partial\Omega} (\mathbf{J}' \cdot \hat{\mathbf{n}})(\mathbf{r}) (\mathbf{J} \cdot \hat{\mathbf{n}})(\mathbf{r}') g(\mathbf{r} - \mathbf{r}') dS' dS \\ & = \int_{\Omega} \mathbf{J}'(\mathbf{r}) \cdot \mathbf{E}_0(\mathbf{r}) d\tau, \end{aligned} \quad (2.5)$$

where $\mathbf{J}' \in H$ is an arbitrary test function.

It is worth noting that (2.4) and (2.5) are also valid in case of anisotropic materials, i.e. when $\sigma + j\omega\chi\varepsilon_0$ is a tensor field.

3. NUMERICAL MODEL

The numerical model is obtained by means of the Galerkin method, once the unknown vector field \mathbf{J} has been properly discretized. Specifically, \mathbf{J} is discretized in term of linear combination of loop and star shape functions, as described in [17, 18, 26, 27, 28]:

$$\mathbf{J} = \sum_{k=1}^{N_L} I_k^L \mathbf{w}_k^L + \sum_{k=1}^{N_S} I_k^S \mathbf{w}_k^S. \quad (3.1)$$

where the \mathbf{w}_k^L s and the \mathbf{w}_k^S s are the *loop* and *star* shape functions, respectively, N_L and N_S are the number of loop and star shape functions and I_k^L and I_k^S are the corresponding Degrees of Freedom (DoFs).

When Ω is simply connected, a loop shape function is related to the edge of the finite element mesh and is given by the curl of the corresponding edge shape function [17]. Each loop shape function represents an *elementary* current loop.

Star shape functions are related to the edges on boundary of the finite element mesh and are also given by the curl of the corresponding edge element. Star shape function corresponds to local *truncated* loops (see Figure 1). Uniqueness of the representation (3.1) can be guaranteed through graph theoretical approaches [17, 26].

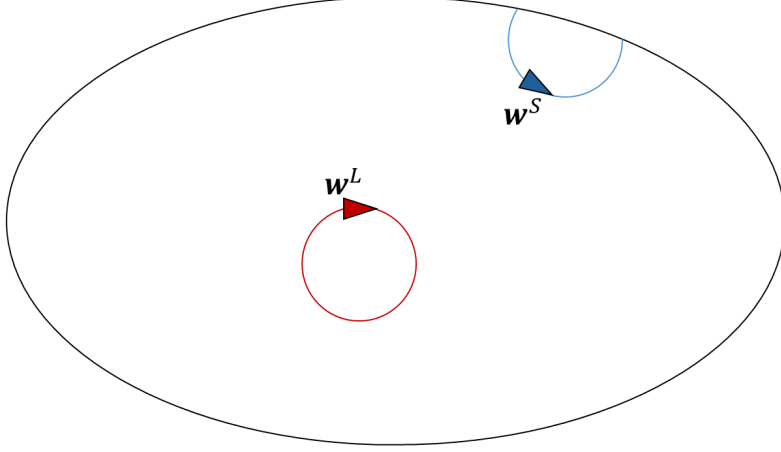


FIGURE 1. Examples of loop (orange) and star (blue) basis functions for a single meta-atom.

The loop and star shape functions satisfy the following properties:

$$\nabla \cdot \mathbf{w}_k^L = 0 \text{ in } \Omega, \mathbf{w}_k^L \cdot \hat{\mathbf{n}} = 0 \text{ on } \partial\Omega \quad (3.2)$$

$$\nabla \cdot \mathbf{w}_k^S = 0 \text{ in } \Omega, \mathbf{w}_k^S \cdot \hat{\mathbf{n}} \neq 0 \text{ on } \partial\Omega, \int_{\Sigma_i} \mathbf{w}_k^S \cdot \hat{\mathbf{n}} dS = 0, \forall i \quad (3.3)$$

The decomposition of the unknown in terms of loop and star components is mandatory to mitigate the so-called low frequency breakdown problem, that is, the dramatic increase of the condition number of the stiffness matrix in the low frequency limit and in the presence of conducting materials that prevent getting an accurate solution [17, 29].

By plugging approximation (3.1) in (2.5) and applying the Galerkin method (projection along the \mathbf{w}_k^L s and the \mathbf{w}_k^S), it results that:

$$\left[\mathbf{R} + j\omega\mu_0\mathbf{L} + \frac{1}{j\omega\varepsilon_0}\mathbf{D} \right] \mathbf{I} = \mathbf{v}_0 \quad (3.4)$$

where

$$\mathbf{R} = \begin{bmatrix} \mathbf{R}^{LL} & \mathbf{R}^{LS} \\ \mathbf{R}^{SL} & \mathbf{R}^{SS} \end{bmatrix}; \mathbf{L} = \begin{bmatrix} \mathbf{L}^{LL} & \mathbf{L}^{LS} \\ \mathbf{L}^{SL} & \mathbf{L}^{SS} \end{bmatrix},$$

$$\mathbf{D} = \begin{bmatrix} \mathbf{0} & \mathbf{0} \\ \mathbf{0} & \mathbf{D}^{SS} \end{bmatrix}; \mathbf{v}_0 = \begin{bmatrix} \mathbf{v}_0^L \\ \mathbf{v}_0^S \end{bmatrix},$$

and

$$\begin{aligned}
R_{ij}^{\alpha\beta} &= \int_{\Omega} \mathbf{w}_i^{\alpha} \cdot [\sigma(\mathbf{r}) + j\omega\chi(\mathbf{r})\varepsilon_0]^{-1} \mathbf{w}_j^{\beta} dV \\
L_{ij}^{\alpha\beta} &= \int_{\Omega} \int_{\Omega} \mathbf{w}_i^{\alpha}(\mathbf{r}) \cdot g(\mathbf{r} - \mathbf{r}') \mathbf{w}_j^{\beta}(\mathbf{r}') dV' dV \\
v_{0,i}^{\alpha} &= \int_{\Omega} \mathbf{w}_i^{\alpha} \cdot \mathbf{E}_0 dV \\
D_{ij}^{SS} &= \int_{\partial\Omega} \int_{\partial\Omega} (\mathbf{w}_i^S \cdot \hat{\mathbf{n}})(\mathbf{r}) g(\mathbf{r} - \mathbf{r}') \times \\
&\quad \times (\mathbf{w}_j^S \cdot \hat{\mathbf{n}})(\mathbf{r}') dS' dS.
\end{aligned}$$

In the following, we define

$$\mathbf{Z} = \mathbf{R} + j\omega\mu_0\mathbf{L} + \frac{1}{j\omega\varepsilon_0}\mathbf{D}. \quad (3.5)$$

and, hence, equation (3.4) reads as

$$\mathbf{Z}\mathbf{I} = \mathbf{v}_0. \quad (3.6)$$

It is worth noticing that the \mathbf{Z} matrix is fully populated.

Hereafter, the volume integral equation (3.6) is solved using an iterative method combining a QR compression method and a preconditioner specifically tailored for metasurfaces.

4. ITERATIVE METHOD AND PRECONDITIONER

When dealing with large-scale problems, direct solvers are impractical, leaving room for iterative solvers, representing the only way to solve the problem. Iterative solvers aim to compute the solution of (3.6) via the repeated computation of the $\mathbf{Z}\mathbf{I}_n$ and $\mathbf{Z}^H\mathbf{I}_n$ products, until the residual falls below a specified threshold.

For large-scale problems, it is unpractical to store the full matrix \mathbf{Z} , so an approximate version obtained by a proper compression method is employed. An iterative method can be conceptualized as a black box (Figure 2) that approximates the solution of a linear system. Given a specified precision for the compressed product $\mathbf{Z}\mathbf{I}$ and a residual threshold, several key outputs are obtained. The first is solution accuracy, which quantifies the error between the numerically computed solution and the “true” solution, that could be determined using a direct method. Another important factor is storage memory, referring to the amount of memory required to evaluate the approximate $\mathbf{Z}\mathbf{I}$ product at the given precision. Additionally, the method’s efficiency is characterized by product complexity, which represents the computational cost of evaluating the $\mathbf{Z}\mathbf{I}$ product. Finally, the number of iterations required to reduce the residual below the threshold provides insight into the convergence behavior of the method.

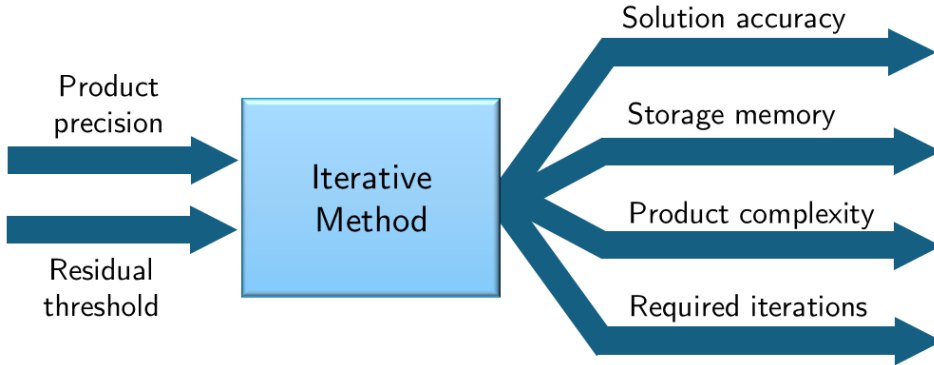


FIGURE 2. Iterative solvers.

In reducing the computational cost, the preconditioners play a key role, since they aim to achieve the target residual value in a smaller number of iterations.

In this work, it is proposed an efficient and effective preconditioner tailored for the geometrical structure of the meta-atoms array. Specifically, the preconditioner consists of the exact inverse of the interaction matrix \mathbf{Z} where the mutual interactions between different meta-atoms are neglected. For the sake of clarity, let the matrix \mathbf{Z} be rearranged and partitioned by meta-atoms, i.e.

$$\mathbf{Z} = \begin{bmatrix} \mathbf{Z}_{1,1} & \mathbf{Z}_{1,2} & \dots & \mathbf{Z}_{1,N} \\ \vdots & & & \vdots \\ \mathbf{Z}_{N,1} & \mathbf{Z}_{N,2} & \dots & \mathbf{Z}_{N,N} \end{bmatrix}, \quad (4.1)$$

where the $\mathbf{Z}_{i,j}$ refers to the mutual interaction between meta-atom i and j , and N is the total number of meta-atoms. The block partition of (4.1) is obtained by ordering the unknowns by meta-atoms, i.e. first the unknowns for the first meta-atom, then the unknowns for the second meta-atom, and so forth.

In this way, the (left) preconditioner used for solving (3.6) iteratively is the inverse of the block diagonal of \mathbf{Z} , i.e. is the inverse of

$$\mathbf{Z}_D = \text{diag}(\mathbf{Z}_{1,1}, \mathbf{Z}_{2,2}, \dots, \mathbf{Z}_{N,N}). \quad (4.2)$$

This preconditioner solves exactly (3.6) when the interactions between meta-atoms are negligible, i.e. the meta-atoms are isolated.

The computational cost for evaluating this preconditioner increases only linearly with the total number of meta-atoms N , and reduces to $O(1)$ if all the meta-atoms are identical. Indeed, in this latter case, it is possible to use the same finite element mesh for each meta-atoms and, therefore, it results that $\mathbf{Z}_{1,1} = \dots = \mathbf{Z}_{N,N}$. Moreover, the computational cost for computing the preconditioner depends on the number N_p of DOFs present in one particle, only, and it results that (i) the number of operations for the factorization of the preconditioner is $O(N_p^3)$, (ii) the memory required to store the factorization of the preconditioner is $O(N_p^2)$, and (iii) the

number of operations to evaluate the preconditioner in the iterative scheme is $O(N_p^2)$.

5. THE QR-RECURSIVE METHOD FOR A META-ATOMS ARRAY

The core of the iterative method lies in approximating the $\mathbf{Z}\mathbf{I}$ matrix-by-vector product in a fast and accurate manner.

The proposed approach is based on the QR-recursive method, which has been successfully applied to MQS problems [22, 23], and here is adapted to a metasurface made by possibly many meta-atoms. In the following, we briefly summarize the main aspects of the method, highlighting its novelty when applied to an array of meta-atoms.

The key concepts of the method are (i) the distinction of near and far distance interaction, (ii) the efficient compression via a low-rank QR-decomposition of the far distance interactions, and (iii) a recursive subdivision scheme.

5.1. Far and near distance interactions. The classification in terms of near and far distance interactions is a relative concept related to a prescribed grid. Specifically, given a regular grid (see Figure 3) superimposed to the metasurface, the interaction between meta-atoms that belong to the same block or a near block are classified as near, while interactions between non-adjacent blocks are classified as far.

Definition. *Two blocks of the grid are near each other if they share at least one node.*

For instance, matrix \mathbf{Z} when partitioned block-wise according to the grid of Figure 3, presents the near interaction blocks in red and the far interaction blocks in green. Matrix \mathbf{Z} can be written as

$$\mathbf{Z} = \mathbf{Z}_F^{(1)} + \mathbf{Z}_N^{(1)}, \quad (5.1)$$

where $\mathbf{Z}_F^{(1)}$ is the matrix made by only the far interactions (green block), while $\mathbf{Z}_N^{(1)}$ consists of only the near distance interactions (red blocks). The superscript highlights that the far-near splitting is at the first grid level. In formal terms, it results that

$$\mathbf{Z} = \mathcal{F}_F^{(1)}\mathbf{Z} + \mathcal{F}_N^{(1)}\mathbf{Z}, \quad (5.2)$$

where $\mathcal{F}_F^{(1)}$ is the linear operator selecting only the far distance interactions

$$\left(\mathcal{F}_F^{(1)} : \mathbf{Z} \mapsto \mathbf{Z}_F^{(1)}\right),$$

while $\mathcal{F}_N^{(1)}$ selects only the near distance interactions

$$\left(\mathcal{F}_N^{(1)} : \mathbf{Z} \mapsto \mathbf{Z}_N^{(1)}\right).$$

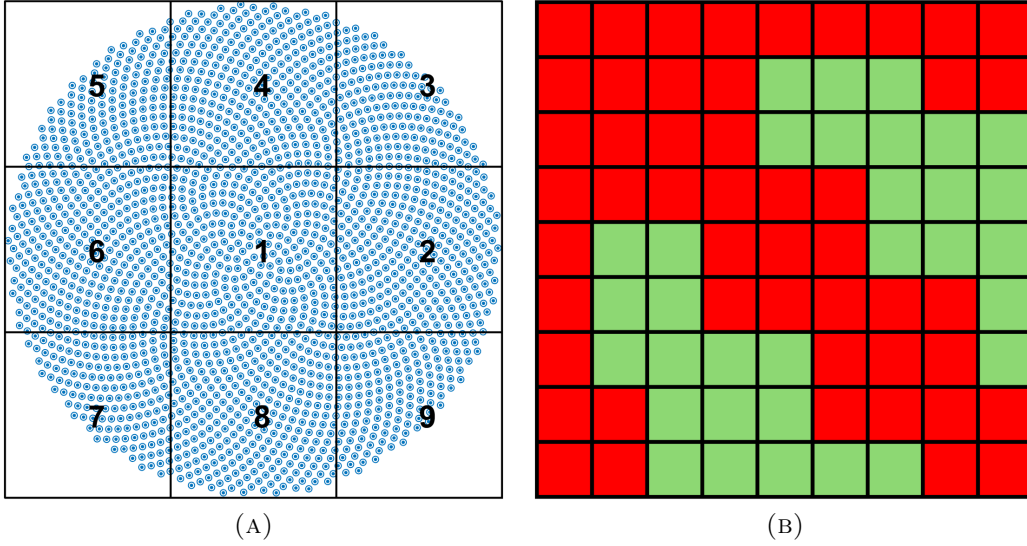


FIGURE 3. Left: the meta-lens together with the grid (black) defining the blocks at the first grid level. Right: matrix \mathbf{Z} partitioned according to the 9 blocks of meta-atom shown at left. Far distance interactions are marked in green, while near distance interactions are marked in red.

5.2. The low-rank QR-decomposition. The far-near distance splitting is very convenient because each individual block accounting for far distance interactions (green blocks in Figure 3) has a rank significantly lower than the size of the block itself, and it can be efficiently compressed via a low-rank QR-decomposition. Moreover, this rank decreases when the distance between the blocks increases.

Let $\left(\mathbf{Z}_F^{(1)}\right)_{i_1, j_1}$ be the $i_1 j_1$ -th block of matrix $\mathbf{Z}_F^{(1)}$. This block accounts for the interactions between the meta-atoms in block i_1 and the meta-atoms in block j_1 , where i_1 and j_1 are far distance blocks. Matrix $\left(\mathbf{Z}_F^{(1)}\right)_{i_1, j_1}$ can be accurately approximated within a prescribed tolerance ε , using a low-rank QR decomposition:

$$\left(\mathbf{Z}_F^{(1)}\right)_{i_1, j_1} \approx \mathbf{Q}_{i_1, j_1}^{(1)} \mathbf{R}_{i_1, j_1}^{(1)}. \quad (5.3)$$

In equation (5.3) $\left(\mathbf{Z}_F^{(1)}\right)_{i_1, j_1}$ is a $m \times n$ matrix, $\mathbf{Q}_{i_1, j_1}^{(1)}$ is a $m \times r$ matrix, and $\mathbf{R}_{i_1, j_1}^{(1)}$ is a $r \times n$ matrix. The integer r represents the rank of the block-to-block interaction matrix $\left(\mathbf{Z}_F^{(1)}\right)_{i_1, j_1}$ corresponding to the prescribed accuracy.

To find the impact of the low-rank QR-approximation of (5.3), it is convenient to evaluate the main computational cost and the memory storage. Specifically,

the evaluation of the matrix-by-vector product $\left(\mathbf{Z}_F^{(1)}\right)_{i_1, j_1} \mathbf{x}_{i_1, j_1}^{(1)}$ with the ordinary formula calls for a computational cost proportional to $C_{\text{dir}} = \mathcal{O}(m \cdot n)$. Similarly, the memory required to store $\left(\mathbf{Z}_F^{(1)}\right)_{i_1, j_1}$ is proportional to C_{dir} . On the contrary, the computation of the matrix-by-vector product via the low-rank QR approximation of (5.3) can be significantly reduced by performing the matrix multiplications in the proper order, i.e. by evaluating $\mathbf{Q}_{i_1, j_1}^{(1)} \left(\mathbf{R}_{i_1, j_1}^{(1)} \mathbf{x}_{i_1, j_1}^{(1)}\right)$. By doing this, the computational cost for computing the matrix-by-vector products is proportional to the smaller quantity $C_{\text{app}} = \mathcal{O}((m+n)r)$ and, similarly, the memory required to store both $\mathbf{Q}_{i_1, j_1}^{(1)}$ and $\mathbf{R}_{i_1, j_1}^{(1)}$ is proportional to the same quantity C_{app} . When $r \ll m, n$, as it is the case for the interactions between blocks of meta-atoms at a far distance, it results that $C_{\text{app}} \ll C_{\text{dir}}$, i.e. $G_{i_1, j_1}^{(1)} \gg 1$, where $G_{i_1, j_1}^{(1)} = C_{\text{dir}}/C_{\text{app}}$ is the compression gain for matrix $\left(\mathbf{Z}_F^{(1)}\right)_{i_1, j_1}$.

5.3. The recursive scheme. From a general perspective, the far/near splitting of (5.1) can be carried out on a coarse grid as well as on a finer grid. The far distance interactions are compressed at the best on coarse grids made by large blocks. On the contrary, the impact of the near distance interactions is reduced on a finer grid made by small blocks. Large blocks are ideal for compressing the far distance interactions, while small blocks are ideal for reducing the number of near distance interactions.

The solution to these conflicting needs comes from a multilevel grid, where each block is subdivided into two parts along each orthogonal direction when moving from one subdivision level to the next. At each level, all the far distance interactions that have not been accounted for at the previous (coarser) level are compressed. The remaining near distance interactions are processed at the next refinement level, where they are partially compressed. For instance, when moving from the first to the second grid level, only $\mathbf{Z}_N^{(1)}$ is processed and split in far and near parts, i.e.

$$\begin{aligned} \mathbf{Z} &= \mathcal{F}_F^{(1)} \mathbf{Z} + \mathcal{F}_N^{(1)} \mathbf{Z} \\ &= \mathcal{F}_F^{(1)} \mathbf{Z} + \mathcal{F}_F^{(2)} \mathcal{F}_N^{(1)} \mathbf{Z} + \mathcal{F}_N^{(2)} \mathcal{F}_N^{(1)} \mathbf{Z}. \end{aligned} \tag{5.4}$$

Similarly, at the third grid level only the near term $\mathcal{F}_N^{(2)} \mathcal{F}_N^{(1)} \mathbf{Z}$ is split in far and near parts. The far distance interactions blocks of $\mathcal{F}_F^{(1)} \mathbf{Z}$ are compressed at the first grid level, while the blocks of $\mathcal{F}_F^{(2)} \mathcal{F}_N^{(1)} \mathbf{Z}$ are compressed at the second grid level and so forth. The near distance interactions are progressively reduced in number, until the last grid level where they are retained without any approximation.

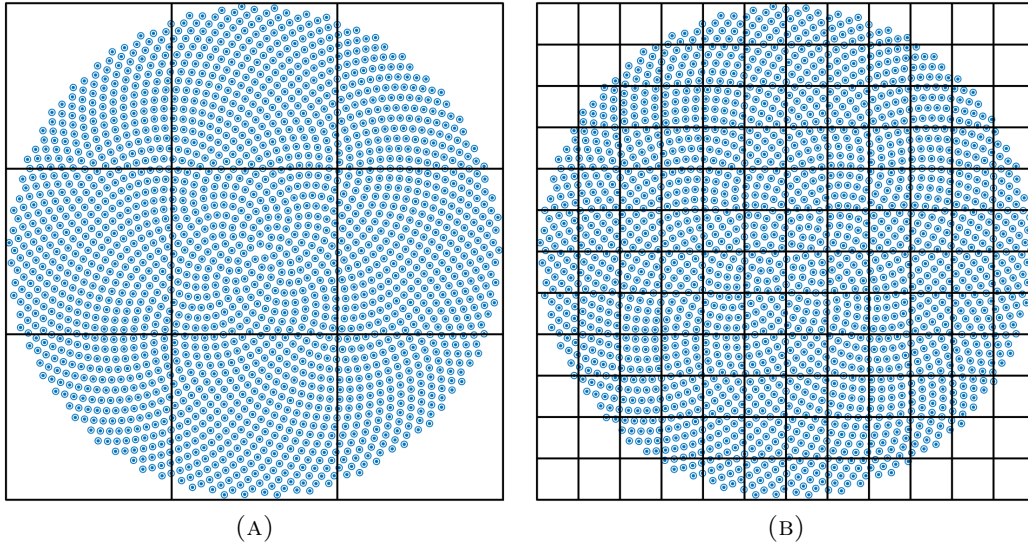


FIGURE 4. The grids for level 1 (left) and level 2 (right).

The overall memory compression G for the complete matrix \mathbf{Z} is given by:

$$G = \frac{N_{\text{dof}}^2}{N_{\text{QR}}}, \quad (5.5)$$

with:

$$N_{\text{QR}} = N_{\text{far}} + N_{\text{near}} = \sum_{l=1}^{N_{\text{level}}} \sum_{i,j} \frac{m_i^{(l)} \times n_j^{(l)}}{G_{i,j}^{(l)}} + NN_p^2, \quad (5.6)$$

where N_{QR} is the size of the matrix after compression, N_{dof} is the total degrees of freedom, N_{level} is the number of grid levels, and $\left(\mathbf{Z}_F^{(l)}\right)_{i,j}$ has dimensions $m_i^{(l)} \times n_j^{(l)}$. The compression gain is inversely proportional to the required storage memory.

5.4. The metasurface. The proposed approach has been tailored for a metasurface made by an array of meta-atoms. Specifically, three ad-hoc customizations have been introduced and summarized below.

First, each meta-atom provides an individual unit where all of its DoFs are attributed to the same block of a given grid level. As discussed in B, splitting a meta-atoms in smaller parts does not provide any benefit from the computational point of view. Therefore, each meta-atom, as a whole, is attributed to the block that contains its barycenter, at a given grid level.

Second, the finer grid level is chosen to have at most one meta-atoms per block to get \mathbf{Z}_N with the smaller number of nonzero elements. In this manner, it results that $\mathbf{Z}_N = \mathbf{Z}_D$

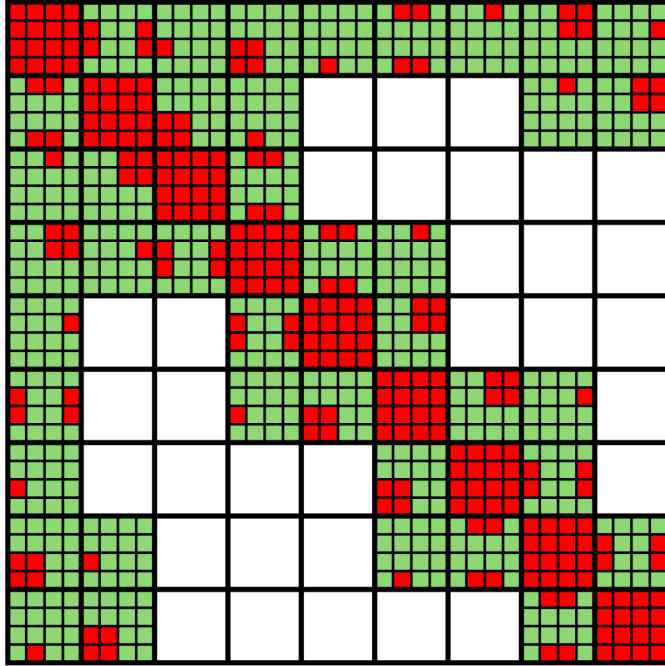


FIGURE 5. Matrix \mathbf{Z} partitioned according to the 36 blocks at the second grid level. The new far distance interactions are marked in green, the current near distance interactions are marked in red, and the far distance interactions compressed at the previous level are marked in white.

Third, at the finer grid level, all the mutual interactions between distinct meta-atoms are compressed. This is because, thanks to the physical properties of the problem, the mutual interaction between distinct meta-atoms exhibits a rank deficiency.

6. NUMERICAL VALIDATION

This section demonstrates the effectiveness of the proposed method through numerical validation, focusing on electromagnetic scattering problems involving electrically large metasurfaces. Following the framework discussed in Section 3 and illustrated in Figure 2, we validate the proposed approach by analyzing computational time, solution accuracy, and memory usage as a function of the precision prescribed for the computation of the matrix-by-vector products.

The numerical validation is organized into several subsections, each addressing specific aspects of the method. After providing a detailed description of the test scenarios in Section 6.1, we first demonstrate the consistency of the proposed method. We show that both the memory requirements and solution accuracy scale with the precision prescribed for evaluating the matrix-by-vector products (Section

6.2). Subsequently, Section 6.3 analyzes the overall performance of the approach, particularly highlighting the memory usage and the number of iterations required by the iterative solver, as the number of degrees of freedom increases. Finally, the efficiency of a parallel implementation is evaluated, with particular care paid to critical aspects such as load balancing across computational resources.

All numerical experiments were performed on a shared memory computing architecture (see details in Table 4). For the sake of consistency, each computation was performed using 64 cores (MPI processes).

The results presented throughout this section employ the GMRES method [30] as iterative solver, paired with the preconditioner described in Section 4. The GMRES was selected because of its superior stability in the reduction of the residual, if compared to other iterative solvers, such as BICGSTAB. The maximum iteration count was set to 5000 without restarts, and convergence was numerically achieved for a residual below a threshold of 1×10^{-4} .

TABLE 1. Machine used for computation

Specification	Details
Machine	HPE Proliant DL380 Gen10
CPU	Intel(R) Xeon(R) Gold 6338 CPU @ 2.00GHz
Nodes	2
Cores per Node	32
L2 Cache	80 MiB
RAM	2 TB

6.1. Description of the cases of interest. The investigated metasurfaces, shown in Fig. 6, consist of arrays formed by replicating identical meta-atoms, of spherical shape. These spheres are arranged in an aperiodic structure known as Vogel’s spiral [31]. This spiral arrangement is convenient for testing because individual meta-atoms can be added one by one without significantly altering the array density. Additionally, varying the number of meta-atoms modifies the array size, facilitating the investigation of the method’s performance across different electrical lengths (ratios between the radius of the array and the free-space wavelength of the incident field). The centers of the spheres for the Vogel’s spiral are located at $(x_i, y_i, 0) = r_i (\cos(i\alpha), \sin(i\alpha), 0)$, for $i = 1, \dots, N$, where N is the number of meta-atoms, $r_i = c\sqrt{i}$, $c = R\sqrt{3}$ is a constant scaling factor, R is the radius of each sphere, $\alpha = 2\pi/\phi^2$ is the golden angle, and $\phi = (1 + \sqrt{5}/2)$ is the golden ratio. Four distinct arrays are analyzed, each composed of spheres with a radius of $R_s = 100$ nm, arranged in configurations of $N = 100, 500, 1000$, and 2000

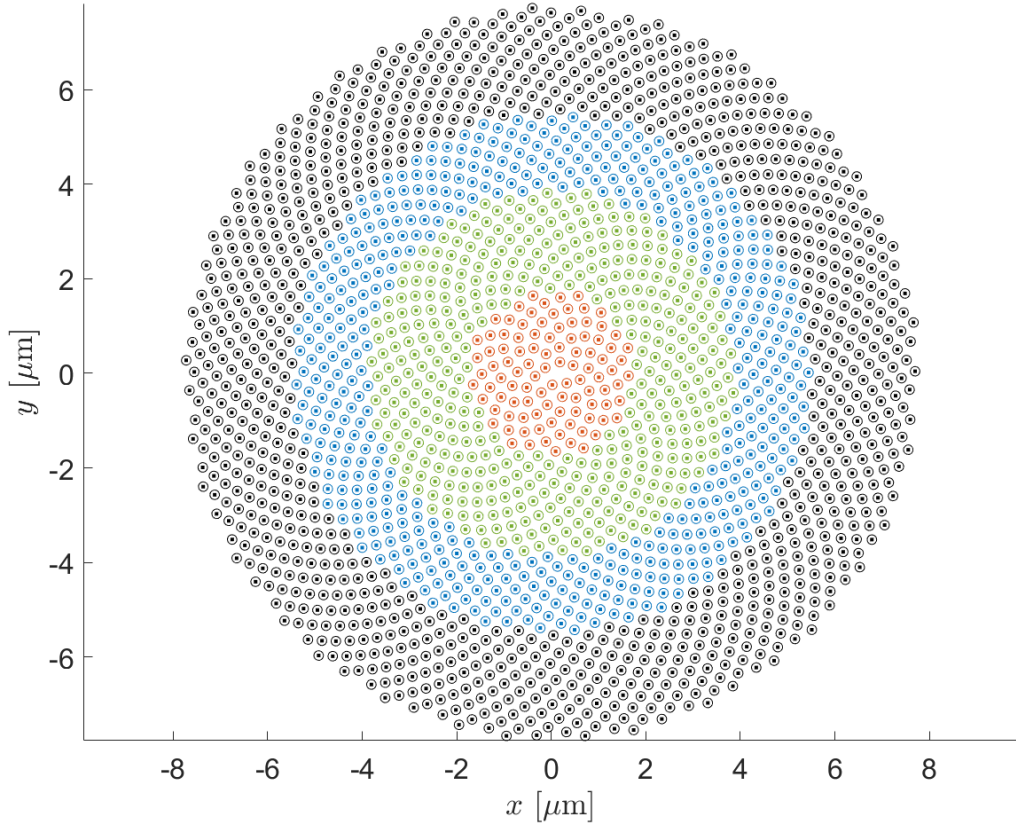


FIGURE 6. The four configurations considered in this paper. Each one is obtained by adding a certain number of meta-atoms to the previous one. Red $N = 100$; green $N = 500$; blue: $N = 1000$; black: $N = 2000$. The array radii are $1.73 \mu\text{m}$, $3.87 \mu\text{m}$, $5.48 \mu\text{m}$, $7.75 \mu\text{m}$, respectively

meta-atoms. The smallest array ($N = 100$) is suitable for direct numerical analysis, serving as a reference case to validate the accuracy and consistency of the proposed numerical method by means of a direct solver, as detailed in the subsequent subsection. From the numerical perspective, all spheres share the same identical finite elements mesh. Table 2 summarizes the main data for each array configuration.

The incident field is a plane wave at a frequency of $f = 5 \times 10^{14}$ Hz, corresponding to a wavelength of 600 nm. The spheres are made of gold [32] characterized by a relative permittivity at the prescribed frequency f of $\varepsilon_r = -9.428 + 1.513i$.

TABLE 2. Mesh data for the cases of interest

Meta-atoms	Points	Elements	Loop	Star	Total DOFs
100	32100	25600	46500	9500	56000
500	160500	128000	232500	47500	280000
1000	321000	256000	465000	95000	560000
2000	642000	512000	930000	190000	1120000

6.2. Consistency of the Method. As described in Section 3, the effectiveness of the iterative method can be evaluated through three primary metrics: (i) the accuracy of the solution, (ii) the memory compression, and (iii) the reduction in the number of multiplications necessary to compute the matrix-by-vector product $\mathbf{Z}\mathbf{I}$ [33]. Thus, it is crucial to analyze the trade-off between solution accuracy and memory compression, as a function of the prescribed accuracy in the computation of the products via compression. This latter quantity is termed P_c and is defined as:

$$P_c = -\log(\varepsilon_{\text{prod}}),$$

$$\varepsilon_{\text{prod}} = \frac{\|\mathbf{Z}_{\text{QR}}\mathbf{u} - \mathbf{Z}\mathbf{u}\|}{\|\mathbf{Z}\mathbf{u}\|},$$

$$\mathbf{u} = (1 + j)[1, \dots, 1]^T,$$

where \mathbf{Z}_{QR} represents the stiffness matrix after compression. The solution accuracy, denoted as A_s , is defined by means of the relative error with respect to the reference solution:

$$A_s = -\log(\varepsilon_{\text{sol}}),$$

$$\varepsilon_{\text{sol}} = \frac{\|\mathbf{J}_{\text{QR}} - \mathbf{J}_{\text{ref}}\|}{\|\mathbf{J}_{\text{ref}}\|},$$

where \mathbf{J}_{ref} represents the induced polarization density obtained via a direct method, i.e. LU decomposition, and \mathbf{J}_{QR} denotes the solution achieved using the proposed iterative method method of Section 5.

The numerical results for the reference case of 100 meta-atoms are shown in Figure 7. As expected, increasing the input accuracy leads to a reduced compression gain and improved solution precision, clearly demonstrating the inverse relationship between these two metrics.

6.3. Performances of the Method. The performances of the proposed method are evaluated by examining two primary metrics: the number of iterations required by the iterative solver (GMRES) to solve equation (3.6) and the compression gain as a function of the number of meta-atoms.

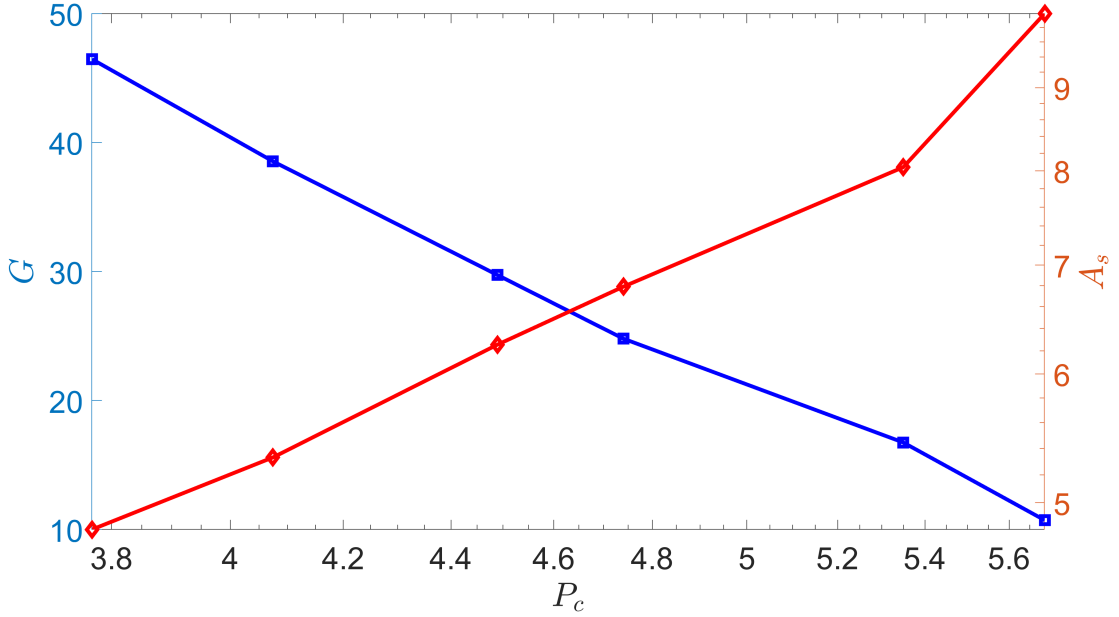


FIGURE 7. Method consistency: Gain G (blue line) and precision A_s (red line) versus accuracy QR-recursive method.

Figure 8 presents the progression of the relative residual norm throughout the GMRES iterations, for arrays containing 100, 500, 1000, and 2000 meta-atoms. As expected, the number of iterations grows when increasing the number of degrees of freedom (DoFs). Remarkably, even the largest scenario (2000 spheres) with approximately 1.1 million unknowns requires only 2600 iterations, clearly demonstrating the efficiency of the method. To further highlight the impact of the preconditioning strategy, we repeated the computation for the array containing 100 particles without using any preconditioner. In this case, the GMRES solver required 9067 iterations, compared to 53 iterations when the proposed preconditioner is employed.

Alternative preconditioners, such as incomplete LU decomposition or sparse approximate inverses [34], could potentially reduce iteration counts but at prohibitive costs in terms of both construction and storage, making them unsuitable for large and dense linear systems.

Performance in memory usage is assessed through the compression gain G , defined in equation (5.5), as a function of the number of unknowns. Figure 9 illustrates how the compression gain improves with increasing meta-atom counts.

To further characterize the compression behavior, Figure 10 reports the compression gain of the individual interaction blocks arising in the recursive partitioning of the matrix \mathbf{Z} , shown as a function of the block size, i.e. occupied memory. The results in Figure 10 refer to the largest configuration considered in this work,

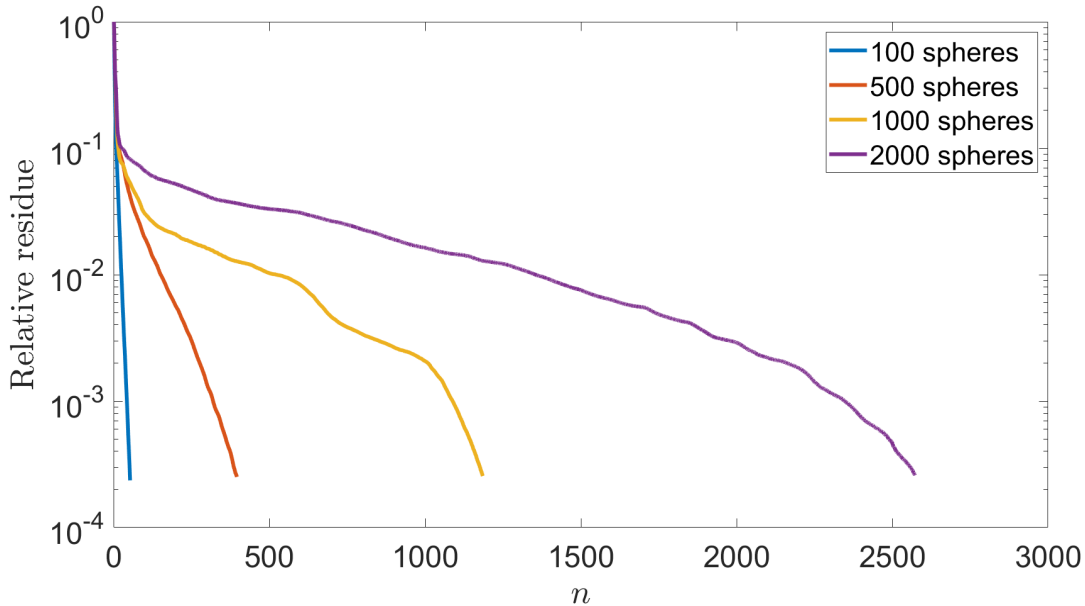


FIGURE 8. Relative residual norm versus the number of GMRES iterations for different meta-atom configurations.

namely the array composed of 2000 particles and QR tolerance $\varepsilon = 10^{-3}$, for which the effect of the compression is most evident.

6.4. Efficiency of the Parallelization Method. Three key factors determine the efficiency of the parallelization strategy: (i) balancing of the computational load during the assembly of the stiffness matrix, (ii) balancing of the memory required to evaluate the matrix-by-vector products, and (iii) balancing of the computation time required to evaluate the matrix-by-vector product. Computational load balancing is essential to ensure an even distribution of the computational workload, maximizing speedup in the construction of the compressed operator. Similarly, memory balancing plays a critical role, particularly in high-performance computing (HPC) environments where identical nodes are used. A well-balanced memory distribution prevents bottlenecks and allows efficient resource scaling as computational demand increases. Furthermore, balancing the computation time during the matrix-by-vector product is mandatory to achieve optimal speedup and enable efficient scalability as the number of processes increases. A suboptimal yet effective algorithm was implemented to distribute the workload efficiently, as detailed in C.

Table 3 shows some statistics on the distribution of the computational load during the assembly of the matrix, in terms of the number of interactions assigned to each processor. Specifically, it includes the average number of interactions

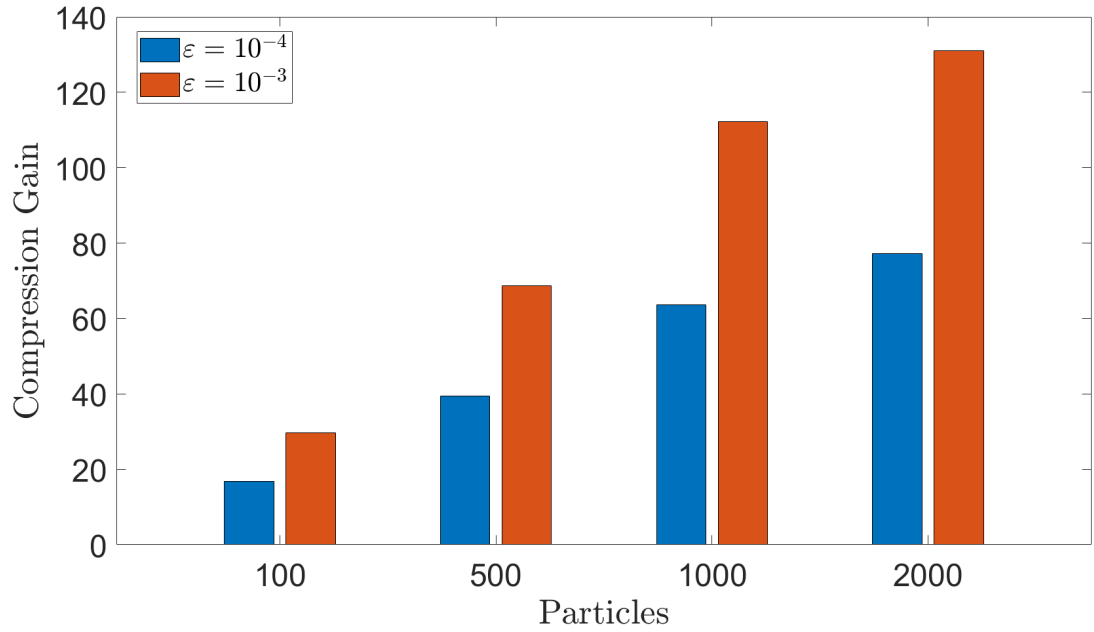


FIGURE 9. Compression gain as a function of the number of meta-atoms, at different values of QR tolerance ε (see Section 5.2).

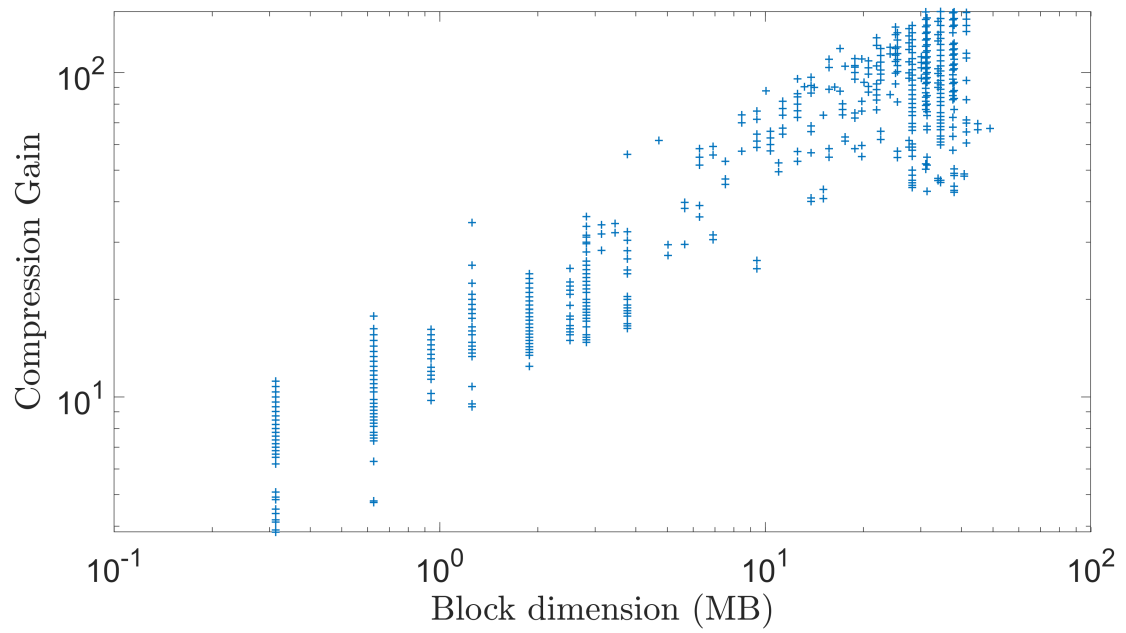


FIGURE 10. Compression gain as a function of the blocks size.

assigned to each processor μ_a , the standard deviation of the number of interactions per processor σ_a , and the normalized standard deviation σ_a/μ_a . The low values of the normalized standard deviation indicate an excellent balance achieved during the assembly phase, ensuring an even distribution of computational efforts across processors.

TABLE 3. Mean value μ_a of the number of interactions assigned to each processor during assembly, corresponding standard deviation σ_a , and normalized standard deviation σ_a/μ_a .

Meta-atoms	Total interactions	μ_a	σ_a	σ_a/μ_a
100	9900	155	0.47	3.00×10^{-3}
500	249500	3898	0.50	1.28×10^{-4}
1000	999000	15609	0.49	3.13×10^{-5}
2000	3986943	62296	0.13	2.00×10^{-6}

Table 4 shows similar statistics but related to the memory allocation per processor, including the average value μ_m , the standard deviation σ_m , and the normalized standard deviation σ_m/μ_m . Even for this aspect, the consistently low values of the normalized standard deviation confirm that the memory distribution remains well-balanced, preventing potential bottlenecks in large-scale computations.

TABLE 4. Average allocated memory μ_m per processor, corresponding standard deviation σ_m , and normalized standard deviation σ_m/μ_m for different test cases with varying numbers of meta-atoms.

Meta-atoms	Total memory (GB)	μ_m (GB)	σ_m (GB)	σ_m/μ_m
100	1.57	0.024	4.90×10^{-3}	0.198
500	16.99	0.265	1.05×10^{-2}	0.040
1000	41.66	0.651	1.84×10^{-2}	0.028
2000	142.67	2.229	2.92×10^{-2}	0.013

6.5. Timing Information. The construction process of the compressed matrix-by-vector operator involves two main steps: (i) local matrix assembly, and (ii) subsequent compression employing the full-cross approximation technique [35]. First, the assembly times required to construct the operator are shown in Table 5 for the scenarios considered. It is evident that, as the size of the array increases, the compression time becomes a significant fraction of the overall duration of the assembly.

TABLE 5. Assembly Time for various array sizes.

Array Size	Assembly (s)	Compression (s)
100	727	70
500	11579	164
1000	41012	11568
2000	116211	65369

TABLE 6. Performance analysis of different stages of the GMRES algorithm across multiple problem sizes (100 to 2000). Values marked with an asterisk (*) indicate extrapolated estimates. All reported timings are expressed in seconds.

Case	100	500	1000	2000	
N_{prd}	number of matrix products (\mathbf{Zx})	107	793	2371	5151
N_{pcnd}	number of preconditioner applications	54	397	1186	2576
ρ_{prd}	\mathbf{Zx} product speed-up	13.98	53.52	95*	96*
$t_{\text{prd}}^{\text{QR}}$	overall QR product $\mathbf{Z}_{\text{QR}}\mathbf{x}$ time	1.15	77.6	530	4.47×10^3
$t_{\text{prd}}^{\text{ord}}$	overall ordinary \mathbf{Zx} product-time	16.03	4.15×10^3	4.97×10^4 *	4.31×10^5 *
t_{pcnd}	overall preconditioner application time	2.42×10^{-1}	11.68	65	282
t_{Kryl}	Krylov algebraic operations Time	17.09	259	4.12×10^3	5.68×10^4
$t_{\text{tot}}^{\text{QR}}$	QR-GMRES overall exc. time	18.48	349	4.71×10^3	6.16×10^4
$t_{\text{tot}}^{\text{ord}}$	Ordinary GMRES overall exc. time	33.36	4.42×10^3	5.38×10^4 *	4.88×10^5 *
ρ_{GMRES}	overall GMRES speed-up	1.8	12.68	11.42*	7.93*

Second, Table 6 provides an in-depth analysis of inversion timing, focusing on the most computationally demanding operations: (i) matrix-by-vector product (\mathbf{Zx}), (ii) preconditioner application ($\mathbf{P}^{-1}\mathbf{y}$), and (iii) Krylov subspace algebraic manipulations necessary for obtaining the minimal solution. We implemented a loop employing the Arnoldi process to minimize the residual error iteratively. It is worth noting that an inefficient preconditioner results in a quadratic growth of the dimension of the Krylov subspace, thus significantly slowing the convergence. To assess the efficiency of the proposed approach, Table 6 compares the GMRES inversion with and without the QR-recursive compression. The reference implementation without QR-recursive compression, referred to *ordinary* implementation, utilizes optimized PBLAS routines to ensure peak efficiency. The presented results clearly illustrate substantial performance gains due to the proposed QR-recursive compression technique. Specifically, the ratio ρ_{prd} of the computation times between ordinary and compressed matrix-by-vector products during the GMRES inversion, demonstrates approximately a hundred-fold acceleration. However, this significant compression translates to an overall GMRES execution speed-up of approximately tenfold compared to the standard GMRES implementation. Thus, the total performance gain does not scale linearly with the compression improvement observed in the matrix products. This discrepancy arises primarily due to limitations in

the efficiency of the preconditioner. Despite this limitation, expanding the Krylov subspace remains indispensable for ensuring high solution accuracy.

7. CONCLUSION

We proposed a fast and robust integral equation solver specifically designed for efficiently handling electrically large particle arrays, extending to linear sizes of many (dozens) wavelengths, a scenario frequently encountered in electromagnetic modeling of metasurfaces and metalenses. Our method integrates a novel QR-recursive compression technique within a volume integral equation (VIE) framework, leveraging an iterative solver coupled with a preconditioner explicitly tailored to exploit the geometric structure of the array. This combination significantly accelerates the iterative solver, maintaining high accuracy. This represents a first and key contribution in view of the simulation of suitable large-scale electromagnetic problems where the scatterer extends for thousands of wavelengths.

Our numerical experiments validated the consistency and scalability of the proposed approach.

We identified and analyzed the three critical factors that dictate the efficiency of our parallelization strategy: (i) balancing of the computational load during the assembly of the stiffness matrix, (ii) balancing of the memory required to evaluate the matrix-by-vector products, and (iii) balancing of the computational time required during the matrix-by-vector products.

By analyzing the scattering from finite arrays of spheres and performing comparative studies against conventional iterative VIE solvers without compression, we quantitatively demonstrated that the proposed QR-recursive compression, combined with a proper pre-conditioner and the GMRES iterative method, achieves approximately a tenfold reduction in computational time, plus substantial memory savings. Our extensive validation further confirmed the solver’s effectiveness even for scenarios involving millions of degrees of freedom, where previously employed VIE approaches are impractical.

These findings highlight that our proposed solver represents a highly valuable computational tool, uniquely positioned to significantly advance the analysis and design capabilities in the field of metasurfaces and complex electromagnetic systems.

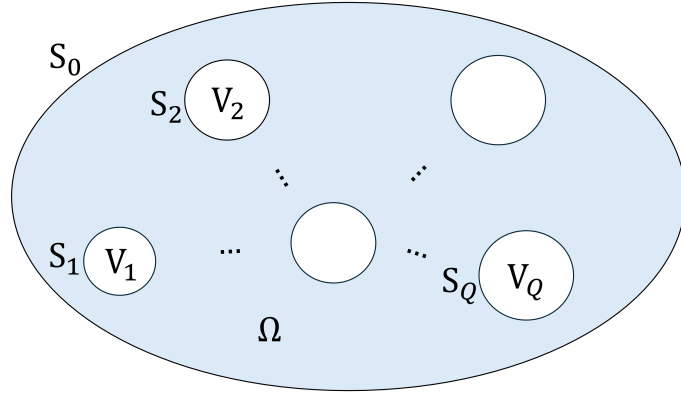
8. ACKNOWLEDGMENT

This work was supported by the Italian Ministry of University and Research under the PRIN-2022, Grant Number 2022Y53F3X “Inverse Design of High-Performance Large-Scale Metalenses”.

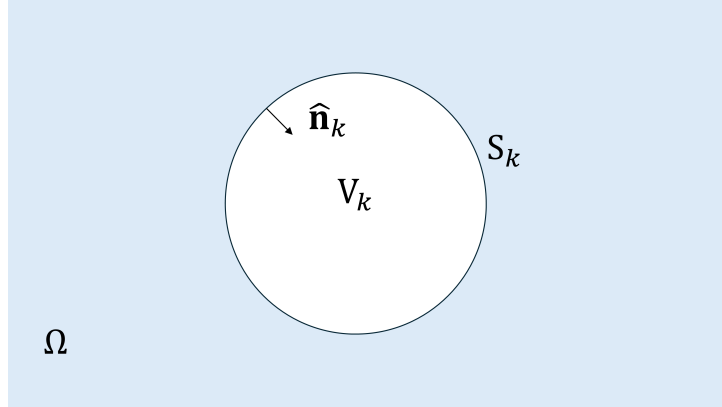
APPENDIX A. PROPERTIES OF \mathbf{J}

This Appendix reviews the main properties of the unknown vector field \mathbf{J} as defined in (2.1) and introduced in [17, 18, 26].

Without loss of generality, let's Ω be made by one meta-atom, only. Aside from being a connected domain, this meta-atom may have an arbitrary topology. For example, the boundary $\partial\Omega$ is assumed to be the union of one or more distinct connected components S_0, \dots, S_Q , where S_0 is the outer boundary while S_1, \dots, S_Q are the boundaries of cavities internal to Ω (see Figure 11(a)). The volumetric region occupied by each cavity and bounded by S_k is denoted as V_k .



(A)



(B)

FIGURE 11. Domain Ω and its internal cavities V_1, V_2, \dots, V_Q (top) and particular of the cavity V_k with its boundary S_k and the normal unit vector $\hat{\mathbf{n}}_k$ (bottom).

The main assumptions are that (i) the material properties σ and χ are constant in each meta-atom, (ii) that each meta-atom is free from source charges in Ω , and

(iii) its cavities V_1, \dots, V_Q , if any, are free from source charges. These assumptions are met in the majority of meta-surfaces occurring in practice.

First, \mathbf{J} is divergence-free. Indeed, it results that

$$\nabla \cdot \mathbf{J} = (\sigma + j\omega\chi)\nabla \cdot \mathbf{E} \quad (\text{A.1})$$

$$= \frac{\sigma + j\omega\chi}{\varepsilon_0(1 + \chi)}\nabla \cdot \mathbf{D} \quad (\text{A.2})$$

$$= 0, \quad (\text{A.3})$$

where the first two equalities come from the material properties σ and χ being constants, while the latter equality comes from the absence of source charge in Ω .

On the boundary of cavity V_k (see Figure 11(b)), the unpaired surface charge density ρ_S^U is responsible for a jump of the normal component of the conduction current $\sigma\mathbf{E}$ and of the electric displacement \mathbf{D} (see [36]):

$$\sigma\mathbf{E}_- \cdot \hat{\mathbf{n}}_k = j\omega\rho_S^U \text{ on } S_k \quad (\text{A.4})$$

$$\mathbf{D}_+ \cdot \hat{\mathbf{n}}_k - \mathbf{D}_- \cdot \hat{\mathbf{n}}_k = \rho_S^U \text{ on } S_k, \quad (\text{A.5})$$

where $\mathbf{D}_\pm(P) = \lim_{h \rightarrow 0^+} \mathbf{D}(P \pm h\hat{\mathbf{n}}_k)$ and $\mathbf{E}_\pm(P) = \lim_{h \rightarrow 0^+} \mathbf{E}(P \pm h\hat{\mathbf{n}}_k)$, for any point P on S_k .

Second, neutrality of the surface charge is achieved on the boundary of each cavity:

$$\int_{S_k} \mathbf{J}_- \cdot \hat{\mathbf{n}}_k dS = 0, \quad \forall k = 1, \dots, Q. \quad (\text{A.6})$$

Indeed, in cavity V_k , from the divergence theorem, it results that:

$$0 = - \int_{V_k} \nabla \cdot \mathbf{D} d\tau \quad (\text{A.7})$$

$$= \int_{S_k} \mathbf{D}_+ \cdot \hat{\mathbf{n}}_k dS \quad (\text{A.8})$$

$$= \int_{S_k} \rho_S^U dS + \int_{S_k} \mathbf{D}_- \cdot \hat{\mathbf{n}}_k dS \quad (\text{A.9})$$

$$= \frac{\sigma + j\omega\varepsilon}{j\omega} \int_{S_k} \mathbf{E}_- \cdot \hat{\mathbf{n}}_k dS \quad (\text{A.10})$$

$$= \frac{\sigma + j\omega\varepsilon}{j\omega(\sigma + j\omega\varepsilon_0\chi)} \int_{S_k} \mathbf{J}_- \cdot \hat{\mathbf{n}}_k dS, \quad (\text{A.11})$$

where the first equality comes from the assumption that V_k is free from source charge, the second equality from the divergence theorem, the third equality from (A.5), the fourth equality from (A.4) and the constitutive relationship $\mathbf{D} = \varepsilon\mathbf{E}$, and the last one from (2.1).

Third, charge neutrality is achieved on S_0 , the outer boundary of Ω . Indeed, the divergence theorem yields

$$0 = \int_{\Omega} \nabla \cdot \mathbf{J} d\tau \quad (\text{A.12})$$

$$= \int_{S_k} \mathbf{J}_- \cdot \hat{\mathbf{n}}_k dS + \sum_{k=1}^Q \int_{S_k} \mathbf{J}_- \cdot \hat{\mathbf{n}}_k dS \quad (\text{A.13})$$

$$= \int_{S_k} \mathbf{J}_- \cdot \hat{\mathbf{n}}_k dS. \quad (\text{A.14})$$

APPENDIX B. (NON) SPLITTING THE META-ATOMS

This Appendix shows that the splitting into different blocks of the DoFs of an individual meta-atom is not convenient from the computational point of view.

For the sake of simplicity, it is considered a simple configuration involving only two meta-atoms. Specifically, the performances regarding the computation of the mutual interactions between these two meta-atoms are evaluated in two scenarios. In the first one (Figure 12(left)), the individual DoFs of two meta-atoms are not split into different blocks. In the second one (Figure 12(right)), the individual DoFs of one meta-atom are split into two different blocks.

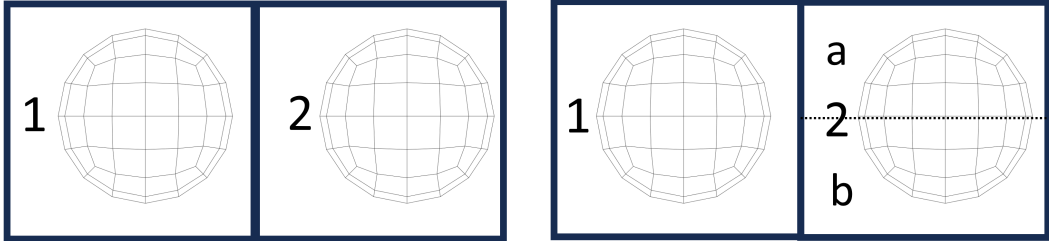


FIGURE 12. Two approaches for computing interaction matrix between two meta-atoms. Left: each meta-atom DOFs are assigned to a single block (1 and 2) : resulting in one matrix interaction. Right: DoFs related to the right meta-atom (the block 2) are split between two subblock blocks (namely a and b): resulting in the sum of two matrices interactions..

In the first case, the mutual interaction between the meta-atoms is approximated and compressed via the QR decomposition as

$$\mathbf{Z}_{1,2} \approx \mathbf{Q}_{1,2} \mathbf{R}_{1,2}, \quad (\text{B.1})$$

where the subscripts refer to the meta-atoms. In the second case, it turns out that

$$\mathbf{Z}_{1,2} = \mathbf{Z}_{1,2a} + \mathbf{Z}_{1,2b} \quad (\text{B.2})$$

$$\approx \mathbf{Q}_{1,2a}\mathbf{R}_{1,2a} + \mathbf{Q}_{1,2b}\mathbf{R}_{1,2b}, \quad (\text{B.3})$$

where $2a$ ($2b$) refers to the DoFs of meta-atom number 2 falling in block a (b).

In Figure 13, the compression gain defined as in (5.5) is shown for the two different approaches as a function of the relative error obtained during the compression. It is worth noting that for a given compression gain, the accuracy achieved without splitting the meta-atom is always higher than that with the splitting.

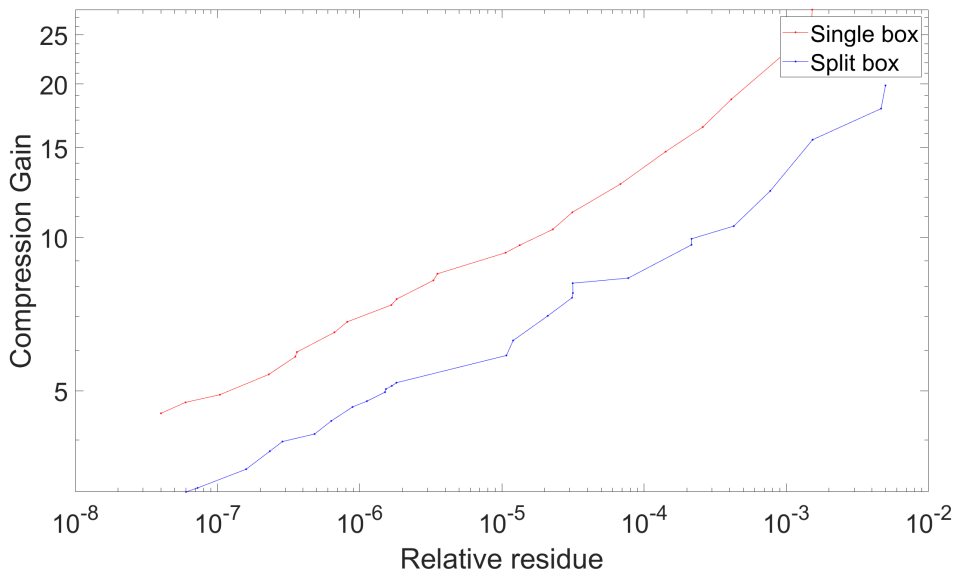


FIGURE 13. Compression Gain vs the approximation error.

APPENDIX C. ALGORITHM FOR DISTRIBUTING BLOCK-BLOCK INTERACTIONS AMONG PROCESSORS

In the following, the parallelization algorithm is reported. The parallelization is performed over QR-recursive block-block interactions, i.e., meta-atom meta-atom interactions. These interactions are assigned statically to MPI processes using a simple greedy least-loaded rule, and the same mapping is reused both during the assembly phase and for each matrix-vector product.

Input:

\mathbf{W}_i : i -th far interaction, $\mathbf{W}_i = (m_i + n_i)r_i$

\mathbf{N}_p : number of processes

Output:**Wei2Proc**(i): i -th interaction process owner**C_k**: k -th process overall load $W_i^s \leftarrow \text{sort}(W_i, \text{descending})$ \triangleright *Zeroing processor loads* \triangleleft **for** $s = 1, \dots, N_p$ **do**┌ $C_s \leftarrow 0$ \triangleright *Assign interactions to processes* \triangleleft **for** $i = 1, \dots, N_{\text{far}}$ **do**┌ $k \leftarrow \arg \min_s C_s$ \triangleright *Find least loaded process*┌ $C_k \leftarrow C_k + W_i^s$ \triangleright *Update k -th process load*┌ **Wei2Proc**(i) $\leftarrow k$ \triangleright *Assign W_i^s to k -th process*

Differently from existing parallelization algorithm (see [37]), the adopted strategy takes advantage of the specific application allowing for a simple strategy able to achieve good load balance (as demonstrated in Section 6.4), while minimization the inter-process communication cost.

REFERENCES

- [1] Holloway C L, Kuester E F, Gordon J A, O'Hara J, Booth J and Smith D R 2012 *IEEE Antennas Propag. Mag.* **54** 10–35 ISSN 1558-4143
- [2] Pfeiffer C and Grbic A 2013 *Physical Review Letters* **110** 197401 ISSN 0031-9007, 1079-7114 URL <https://link.aps.org/doi/10.1103/PhysRevLett.110.197401>
- [3] Silva A, Monticone F, Castaldi G, Galdi V, Alú A and Engheta N 2014 *Science* **343** 160–163 ISSN 0036-8075, 1095-9203
- [4] Altug H, Oh S H, Maier S A and Homola J 2022 *Nature Nanotechnology* **17** 5–16 ISSN 1748-3395 publisher: Nature Publishing Group URL <https://www.nature.com/articles/s41565-021-01045-5>
- [5] Chen H T, Taylor A J and Yu N 2016 *Reports on Progress in Physics* **79** 076401 ISSN 0034-4885 publisher: IOP Publishing URL <https://dx.doi.org/10.1088/0034-4885/79/7/076401>
- [6] Choi M, Park J, Shin J, Keawmuang H, Kim H, Yun J, Seong J and Rho J 2024 *npj Nanophotonics* **1** 1–14 ISSN 2948-216X publisher: Nature Publishing Group URL <https://www.nature.com/articles/s44310-024-00029-2>
- [7] Kang C, Park C, Lee M, Kang J, Jang M S and Chung H 2024 *Nanophotonics* **13** 3765–3792 ISSN 2192-8614 publisher: De Gruyter URL <https://www.degruyter.com/document/doi/10.1515/nanoph-2024-0127/html>
- [8] Yu N and Capasso F 2014 *Nature Materials* **13** 139–150 ISSN 1476-4660 URL <https://www.nature.com/articles/nmat3839>
- [9] Aieta F, Kats M A, Genevet P and Capasso F 2015 *Science* **347** 1342–1345 publisher: American Association for the Advancement of Science URL <https://www.science.org/doi/10.1126/science.aaa2494>
- [10] Lalanne P and Chavel P 2023 *Photoniques* 41–45 ISSN 1629-4475, 2269-8418 number: 119 Publisher: EDP Sciences
- [11] Jin J M 2011 *Theory and computation of electromagnetic fields* (John Wiley & Sons)
- [12] Yee K S and Chen J S 1997 *Antennas and Propagation, IEEE Transactions on* **45** 354–363 ISSN 0018-926X
- [13] Taflov A and Hagness S C 2005 *Computational Electrodynamics: The Finite-Difference Time-Domain Method* 3rd ed (Artech House Publishers)
- [14] Oskooi A F, Roundy D, Ibanescu M, Bermel P, Joannopoulos J D and Johnson S G 2010 *Computer Physics Communications* **181** 687–702 ISSN 0010-4655 URL <https://www.sciencedirect.com/science/article/pii/S001046550900383X>
- [15] Shlager K and Schneider J 1995 *IEEE Antennas and Propagation Magazine* **37** 39–57
- [16] Hughes T W, Minkov M, Liu V, Yu Z and Fan S 2021 *Applied Physics Letters* **119** 150502 ISSN 0003-6951
- [17] Rubinacci G and Tamburrino A 2006 *IEEE Transactions on Antennas and Propagation* **54** 2977 – 2989
- [18] Miano G, Rubinacci G and Tamburrino A 2010 *IEEE Transactions on Antennas and Propagation* **58** 2920 – 2933
- [19] Forestiere C, Gravina G, Miano G, Rubinacci G and Tamburrino A 2023 *IEEE Trans. Antennas Propag.* **71** 6779–6793 ISSN 1558-2221 URL <https://ieeexplore.ieee.org/abstract/document/10154607>
- [20] Corsaro E, Miano G, Tamburrino A, Ventre S and Forestiere C 2024 Multilevel Fast Multipole Algorithm for Electromagnetic Scattering by Large Metasurfaces using Static Mode Representation arXiv:2407.21724 [physics] URL <http://arxiv.org/abs/2407.21724>

- [21] Poirier J R, Borderies P, Mittra R and Varadarajan V 1998 *IEEE Trans. Antennas Propag.* **46** 1169–1175 ISSN 1558-2221
- [22] Rubinacci G, Ventre S, Villone F and Liu Y 2009 *Journal of Computational Physics* **228** 1562–1572 ISSN 0021-9991 URL <https://www.sciencedirect.com/science/article/pii/S0021999108005822>
- [23] Cau F, Chiariello A, Rubinacci G, Scalera V, Tamburrino A, Ventre S and Villone F 2022 *Energies* **15** 3214
- [24] Sayed S B, Liu Y, Gomez L J and Yucel A C 2022 *IEEE Transactions on Antennas and Propagation* **70** 3549–3559
- [25] Guo H, Hu J and Michielssen E 2013 *IEEE Antennas and Wireless Propagation Letters* **12** 31–34
- [26] Forestiere C, Miano G, Rubinacci G, Tamburrino A, Udpa L and Ventre S 2017 *IEEE Transactions on Antennas and Propagation* **65** 1224 – 1235
- [27] Miano G, Rubinacci G and Tamburrino A 2007 *COMPEL - The International Journal for Computation and Mathematics in Electrical and Electronic Engineering* **26** 586 – 599
- [28] Dal Negro L, Miano G, Rubinacci G, Tamburrino A and Ventre S 2009 *IEEE Transactions on Magnetics* **45** 1618 – 1621
- [29] Zhao J S and Chew W C 2000 *IEEE Transactions on Antennas and Propagation* **48** 1635 – 1645
- [30] Saad Y and Schultz M 1986 *SIAM Journal on Scientific and Statistical Computing* **7** 856–869
- [31] Trevino J, Cao H and Dal Negro L 2011 *Nano Letters* **11** 2008–2016 ISSN 1530-6984 URL <https://doi.org/10.1021/nl2003736>
- [32] Johnson P B and Christy R W 1972 *Phys. Rev. B* **6** 4370–4379
- [33] Yu C D, Levitt J, Reiz S and Biros G 2017 Geometry-oblivious fmm for compressing dense spd matrices *Proceedings of the International Conference for High Performance Computing, Networking, Storage and Analysis SC '17* (New York, NY, USA: Association for Computing Machinery) ISBN 9781450351140 URL <https://doi.org/10.1145/3126908.3126921>
- [34] Benzi M 2002 *J. Comput. Phys.* **182** 418–477 ISSN 0021-9991 URL <http://dx.doi.org/10.1006/jcph.2002.7176>
- [35] Kurz S, Rain O and Rjasanow S 2002 *IEEE Transactions on Magnetics* **38** 421–424
- [36] Haus H A and Melcher J R 1989 *Electromagnetic Fields and Energy* (Englewood Cliffs, NJ: Prentice-Hall) ISBN 013249020X
- [37] Li Y, Poulson J and Ying L 2021 *CSIAM Transactions on Applied Mathematics* **2** 431–459